

An early extrasolar planetary system revealed by planetesimal belts in β Pictoris

Yoshiko Kataza Okamoto^{1,2*}, Hirokazu Kataza², Mitsuhiro Honda³, Takuya Yamashita⁴, Takashi Onaka³, Jun-ichi Watanabe⁵, Takashi Miyata⁶, Shigeyuki Sako⁶, Takuji Fujiyoshi⁴ & Itsuki Sakon³

¹Center for Natural Sciences, College of Liberal Arts and Sciences, Kitasato University, 1-15-1 Kitazato, Sagamihara, Kanagawa 228-8555, Japan

²Department of Infrared Astrophysics, Institute of Space and Astronautical Science, Japan Aerospace Exploration Agency, 3-1-1 Yoshinodai, Sagamihara, Kanagawa 229-8510, Japan

³Department of Astronomy, Graduate School of Science, University of Tokyo, 7-3-1 Hongo, Bunkyo-ku, Tokyo 113-0033, Japan

⁴Subaru Telescope, National Astronomical Observatory of Japan, 650 North A'ohoku Place, Hilo, Hawaii 96720, USA

⁵National Astronomical Observatory of Japan, 2-21-1 Osawa, Mitaka, Tokyo 181-8588, Japan

⁶Institute of Astronomy, School of Science, University of Tokyo, 2-21-1 Osawa, Mitaka, Tokyo 181-0015, Japan

* Present address: Institute of Astrophysics and Planetary Sciences, Ibaraki University, Bunkyo 2-1-1, Mito, Ibaraki 310-8512, Japan

β Pictoris (β Pic) is a main-sequence star with an edge-on dust disk^{1–3} that might represent a state of the early Solar System. The dust does not seem to be a remnant from the original protoplanetary disk, but rather is thought to have been generated from large bodies like planetesimals and/or comets^{4,5}. The history and composition of the parent bodies can therefore be revealed by determining the spatial distribution, grain size, composition and crystallinity of the dust through high-resolution mid-infrared observations. Here we report that the sub-micrometre amorphous silicate grains around β Pic have peaks in their distribution around 6, 16 and 30 AU (1 AU is the Sun–Earth distance), whereas the crystalline and micrometre-sized amorphous silicate grains are concentrated in the disk centre. As sub-micrometre grains are blown quickly out from the system by radiation pressure from the central star, the peaks indicate the locations of ongoing dust replenishment, which originates from ring-like distributions of planetesimals or ‘planetesimal belts’.

β Pic is a nearby (19.28 pc = 63 light yr)⁶, young (20 Myr)⁷, A5V Vega-like star. A high-resolution 17.9- μ m image of its inner disk (radius $r < 100$ AU) has revealed the existence of dust rings at 14, 28, 52 and 82 AU (ref. 8). The locations of the rings correspond to the region inside the Edgeworth–Kuiper belt (50 AU) of our Solar System, where the planets are formed. The rings indicate a planetary system containing multiple planets, though the nature of the rings remains an open question. During planetary system formation, the materials in protoplanetary disks experience substantial processing. Whereas silicate grains are observed as amorphous in interstellar space, partially crystallized silicate grains are sometimes found in protoplanetary disks^{9,10} and comets¹¹. Dust emission of β Pic also shows the 9.7- μ m amorphous silicate feature and the 11.2- μ m crystalline olivine ((Mg,Fe)₂SiO₄) feature, like some comets¹². Coexistence of crystalline silicates with icy cold materials in comets is paradoxical, because the crystallization of amorphous silicates by annealing requires high temperatures (>1,000 K)¹³. Investigations of the locations of amorphous and crystalline silicates in β Pic provide key information to help the understanding of the crystallization and evolution of dust grains in an early stage of the planetary disk.

We made 10- μ m-band spectroscopic observations ($\lambda/\Delta\lambda \approx 250$, where λ indicates wavelength) of β Pic with the Cooled Mid-Infrared Camera and Spectrometer (COMICS)^{14–16} on the 8.2-m

Subaru Telescope with high spatial resolution. The obtained spectra are shown in Fig. 1. The spectra for the central part (Fig. 1j–l) are clearly different from the other spectra. They have emission peaks at 10.05, 10.30, 10.40, 11.05 and 11.90 μ m. Three of them match with the Mg-pure crystalline olivine (forsterite, Mg₂SiO₄) peaks (10.06, 10.42 and 11.89 μ m)¹⁷. The 11.24- μ m peak of forsterite in laboratory data¹⁷ can be shifted to 11.1 μ m by the shape effect. The spectra between 8.0 and 13.2 μ m were fitted by a least-squares method with model spectra composed of 0.1- and 2- μ m-radius glassy olivine¹⁸, crystalline forsterite¹⁷, and power-law continuum emission. The 0.1- μ m and 2.0- μ m grains represent small (grain radius $s \leq 1$ μ m) and large ($s \approx$ a few μ m) grains, respectively. The power-law emission takes account of the residual emission, and the index is given as a free parameter. The derived spatial distribution of each dust emission (Fig. 2) indicates that the 2- μ m glassy olivine and the crystalline forsterite are concentrated in the disk centre. In contrast, the 0.1- μ m glassy olivine does not exhibit a central concentration, but has distribution peaks at 6.4 AU in both sides with weak humps around 16 and 29 AU in the northeast side and around 32 AU in the southwest side. Even when the residual continuum is fitted with a grey-body dust emission (emissivity $\epsilon \approx \text{const.}$) or dust emission of $\epsilon \propto 1/\lambda$, the peaks of the 0.1- μ m glassy olivine at 6.4 and 16 AU are unambiguously present. Only in the case of the $\epsilon \propto 1/\lambda$ emissivity are the humps around 30 AU not seen clearly.

In the β Pic system, grains smaller than 1.5 μ m should be blown out, because the ratio of radiation pressure to gravity (β) exceeds unity according to calculation¹⁹ and revised luminosity (8.7 times solar luminosity)⁶. The fact that a large amount of small grains exist around 6.4 AU indicates that small grains are being replenished at this radius at present. The weak distribution peaks at 16 and 30 AU suggest that these two radii are also places of ongoing replenishment of small grains. They correspond to the dust rings seen in 17.9 μ m at 14 and 28 AU (ref. 8).

If the grains are replenished by planetesimal collisions, it is likely that not only small grains but also large grains are simultaneously replenished at the same radii. However, grains of a few micrometres in size fall towards the central star by Poynting–Robertson drag, and are concentrated in the disk centre (grain density $n(r) \propto r^{-1}$) in a steady state²⁰. Convolution of the point spread function (PSF) with the disk emission distribution derived by assuming grain surface density scales as $\Sigma(r) \propto (1/r)r \approx r^0$ and the temperature profile in Fig. 2 accounts for the observed PSF-like distribution of the 2- μ m grains fairly well.

Infalling large amorphous grains will be heated to a temperature high enough to be crystallized near the star by stellar radiation. Crystalline forsterite can be produced by such thermal annealing. Grains of 2- μ m size reach a classical annealing temperature of 1,000 K (ref. 13) at 0.3 AU from the star. A recent paper reported the activation energy required to crystallize Mg₂SiO₄ smokes, suggesting that the crystallization can occur in 3 yr at 800 K (ref. 21); this annealing temperature can be obtained at 0.6 AU. The unresolved profile of the crystalline forsterite (a_3 , defined in Fig. 2 legend) indicates that crystalline forsterite is concentrated in a very compact central region. The upper limit of the crystallinity of the silicate grains replenished at 6.4 AU is estimated as 10% (2σ level), which seems rather low to explain the observed crystalline mass discussed below. These two facts support annealing by the central star. The spectrum taken by the Infrared Space Observatory (ISO) does not show any 20–40- μ m crystalline silicate features²², suggesting that the temperature of crystalline grains (if they exist) is no lower than 500 K, otherwise the 20–40- μ m features would become more than one-third of the 10- μ m features (in Jy). Because the mass absorption coefficient of crystalline forsterite in the 3- μ m region is less than that at 11.24 μ m by more than two orders of magnitude, emission at 3 μ m from forsterite grains is estimated to be less than 0.08 Jy. It is consistent with the ISO spectrum.

What is the replenishing source for the grains around 6.4, 16 and

30 AU? The most likely process is collisions among planetesimals in planetesimal belts similar to the asteroid belt in our Solar System (Fig. 3). The masses of 0.1- μm dust in the belts at 6.4, 16 and 30 AU are all similar to each other (1×10^{16} kg for each of the 6.4, 16 and 30 AU emissions in the northeast side, and 7×10^{16} kg for the whole southwest side). It suggests that three belts supply grains almost equally. The asymmetry of the 6.4-AU small grain enhancement indicates that the 6.4-AU belt is slightly inclined compared to the outer disk (Fig. 3).

Alternatively, evaporation from cometary bodies infalling towards the star could also be a grain replenishment source. It is,

however, difficult to explain by this process the depletion of small grains in the disk centre, the grain replenishment at 16 and 30 AU, and the 0.1- μm grain enhancement at the southwest side at 6.4 AU. Also, grains with large-eccentricity orbits typical of comets are more easily blown out than grains with circular orbits, even if the β value is small. Replenishment in the planetesimal belts is thus the most likely dust supply mechanism in β Pic.

The discovered planetesimal belts may be formed by the gravitational perturbation of planetesimals in unstable orbits due to resonance with possible large planets. In the Solar System, the mean motion resonance plays an important role in the relation

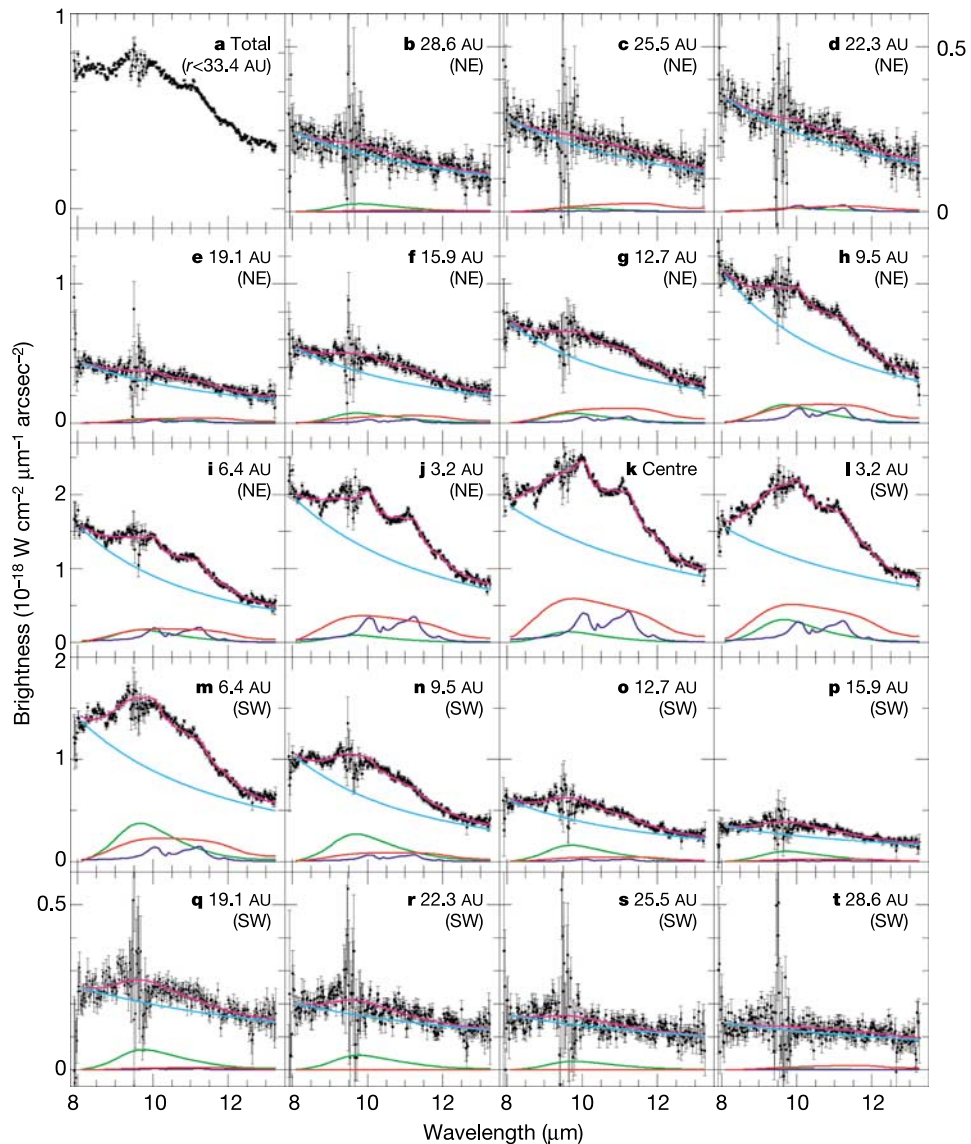


Figure 1 Spectra of β Pic after subtraction of the photospheric emission. **a**, The spectrum integrated along the slit for the $r < 33.4$ AU region. It shows a peak at $11.1\,\mu\text{m}$ and $\sim 9.7\,\mu\text{m}$ and a hump around $12\,\mu\text{m}$ seen in past observations¹². **b–t**, The spectrum for each spatial pixel within 26 AU. The position within the disk is indicated in each panel. Northeast and southwest directions are indicated as NE and SW, respectively. The black points with error bars (s.d.) indicate the observed spectra. The atmospheric ozone absorption significantly degrades the signal to noise (S/N) ratio between 9.3 and $9.9\,\mu\text{m}$. The magenta lines are fitted spectra, and the other coloured lines indicate the contribution from each component: $0.1\text{-}\mu\text{m}$ radius amorphous silicate (green), $2.0\text{-}\mu\text{m}$ radius amorphous silicate (red), crystalline forsterite (blue), and power-law continuum component (cyan). The fitting formula is given in the legend of Fig. 2. The $11.05\text{-}\mu\text{m}$ peak

in the spectra of the disk centre is an unidentified dust feature or line emission overlying the $11.1\text{-}\mu\text{m}$ peak. The observations were long-slit spectroscopy, made on 11 and 12 December 2003 (UT). We used the $0.33''$ -width slit with a position angle of 30° , almost along the outer disk. The pixel scale was $0.165''$. The stellar component is subtracted assuming a $8,200\text{ K}$ blackbody and using the PSF from the standard stars, whose full-width at half-maximum is $0.8''$. Among all the data acquired in more than 3 h of integration time, we have selected $2,983$ -s data taken under good seeing conditions to obtain a spatial resolution as high as possible. For this selection, the spatial profile of each data file was fitted with a gaussian, and data with the standard deviation of the gaussian no larger than $0.4''$ were used.

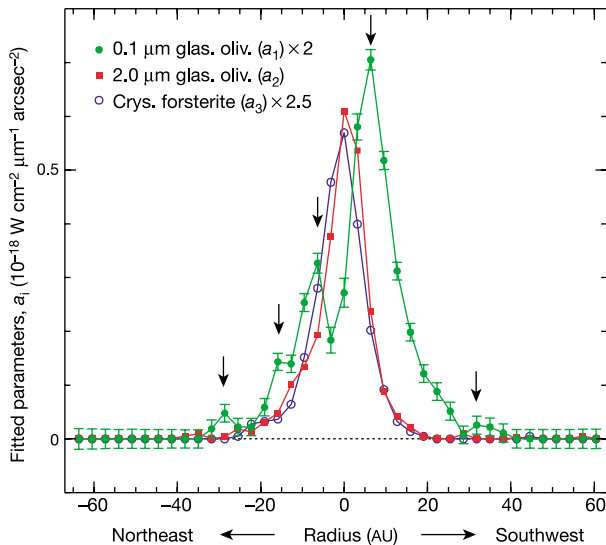


Figure 2 Distribution of each dust emission. The spatial profile of each fit parameter, a_i , which is the brightness of each dust component at $10 \mu\text{m}$ scaled by each normalized mass absorption coefficient, is shown. The fitting formula is given by $F(\lambda) = a_0(\lambda/\mu\text{m})/10 \mu\text{m})^n + \sum_{i=1}^3 a_i \kappa_i(\lambda) B(\lambda, T_i) / B(10 \mu\text{m}, T_i)$, where $F(\lambda)$ is the observed flux at wavelength λ (μm) in $10^{-18} \text{ W cm}^{-2} \mu\text{m}^{-1} \text{ arcsec}^{-2}$, a_i and κ_i are the normalization factors and the mass absorption coefficients normalized as in our recent paper¹⁰, respectively. The normalizing constants in $\text{cm}^2 \text{ g}^{-1}$ for the 0.1 - and 2.0 - μm glassy olivine and crystalline forsterite are $2,372.3$, $1,664.6$ and $2,476.6$, respectively. The suffix i indicates three dust species: 0.1 - μm radius glassy olivine¹⁸ (1; green), 2 - μm radius glassy olivine¹⁸ (2; red), and crystalline forsterite¹⁷ (3; blue). Typical errors for a_2 and a_3 are 0.008 and 0.005 ($10^{-18} \text{ W cm}^{-2} \mu\text{m}^{-1} \text{ arcsec}^{-2}$), respectively. The errors are in s.e. The continuum emission in the spectra is expressed in the power law of index n with the normalization factor a_0 . The temperatures of amorphous grains^{24,8} are assumed to be given by $T_i(\text{K}) = 468(L/s_i)^{0.2} r^{-0.4}$, where L is the luminosity of the central star (8.7 times the solar luminosity)⁶, s_i is the grain radius in μm , and r is the disk radius in AU at the inner side of each pixel. Their temperatures are assumed to be 700 K at the central pixel. The temperature of crystalline forsterite is assumed to be $1,200 \text{ K}$, since the spatial profile is similar to the PSF (only the width of the profile is about 0.8 times of that of the PSF). Black arrows indicate the distribution peaks of 0.1 - μm amorphous silicate grains and the detection of enhancements around 30 AU is marginal. Even if we use the derived distribution of a_3 as the PSF instead of the standard star's profile to subtract the stellar component, the resultant distributions of the components are not changed.

between the planets and the debris belts, such as the asteroid belt and the Edgeworth–Kuiper belt (EKB). The outer and inner edges of the asteroid belt are in $2:1$ and $4:1$ resonance relations with Jupiter, respectively. If the same relations hold for the 6.4 -AU belt around β Pic, the semi-major axis of the planet in resonance and the width of the 6.4 -AU belts are estimated as 12 AU and 3 AU, respectively. The latter value is consistent with the belt width unresolved in our observations. The planet at 12 AU is also in a $3:2$ resonance relation with the 16 -AU belt—like the relation between Neptune and plutinos in the EKB objects.

By assuming that replenished small grains are blown out within the free-fall time (a few to several tens of years), their replenishment rate from each belt is estimated as about 10^{15} – $10^{16} \text{ kg yr}^{-1}$. This is 10^5 – 10^6 times larger than the replenishment rate of the zodiacal dust²³, and there must be a much larger number of planetesimals than asteroids in the present Solar System. The β Pic system is likely to be at a violent planetesimal collision stage in an early solar system.

To estimate the mass of the 2 - μm amorphous and crystalline grains, we assume that the grains are supplied at 6.4 AU as amorphous grains, falling by Poynting–Robertson drag in a steady condition, all being crystallized within the crystallization radius

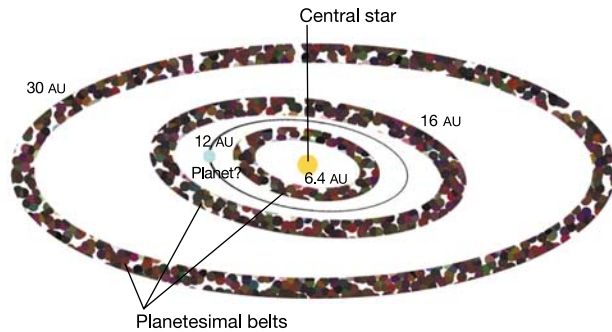


Figure 3 Conceptual view of the discovered planetesimal belts. The locations of the belts are estimated from the dust distribution in Fig. 2. The coloured small dots indicate the planetesimals making up the belts. Planetesimals in the three belts are replenishing amorphous silicate grains by their collisions. The 6.4 -AU belt seems to be inclined compared to the outer disk, as the small grain enhancement around 6.4 AU is larger for the southwest side than for the northeast side (Fig. 2). This asymmetry can be explained by a combination of the inclined position angle of the 6.4 -AU belt and the present slit position slightly shifted towards the southeast. It is supported by the fact that the inner disk ($r < 20$ AU) has been found to be inclined against the outer disk from the mid-infrared images²⁵. The inclination of the 16 -AU belt against the outer disk is derived from the 14 -AU dust ring in the 17.9 - μm image⁸.

r_c , and evaporated at 0.11 AU, where grains reach a temperature of $1,500$ K. If the crystallization temperature is assumed to be 800 K ($r_c = 0.6$ AU)²¹, the estimated dust masses of the (2 - μm) amorphous and crystalline grains are respectively $3 \times 10^{17} \text{ kg}$ and $7 \times 10^{15} \text{ kg}$. Taking account of the uncertainties in the assumed temperature profile (Fig. 2) as well as in the density distribution, this suggests that it is reasonable to surmise that the crystalline grains are formed from the amorphous grains near the central star by the stellar radiation. Detailed self-consistent models are required for more precise discussions. \square

Received 9 April; accepted 17 August 2004; doi:10.1038/nature02948.

1. Gillett, F. C. in *Light on Dark Matter* (ed. Israel, F. P.) 61–69 (Reidel, Dordrecht, 1986).
2. Smith, B. A. & Terrell, R. J. A circumstellar disk around Beta Pictoris. *Science* **226**, 1421–1424 (1984).
3. Pantin, E., Lagage, P. O. & Artymowicz, P. Mid-infrared images and models of the beta Pictoris dust disk. *Astron. Astrophys.* **327**, 1123–1136 (1997).
4. Backman, D. E. & Paresce, F. in *Protostars and Planets III* (eds Levy, E. H. & Lunine, J. I.) 1253–1304 (Univ. Arizona Press, Tucson, 1993).
5. Lecavelier des Etangs, A., Vidal-Madjar, A. & Ferlet, R. Dust distribution in disks supplied by small bodies: is the β Pictoris disk a gigantic multi-cometary tail? *Astron. Astrophys.* **307**, 542–550 (1996).
6. Crifo, F., Vidal-Madjar, A., Lallement, R., Ferlet, R. & Gerbaldi, M. β Pictoris revisited by Hipparcos. Star properties. *Astron. Astrophys.* **320**, L29–L32 (1997).
7. Barrado y Navascues, D., Stauffer, J. R., Song, I. & Caillaud, J.-P. The age of beta Pictoris. *Astrophys. J.* **520**, L123–L126 (1999).
8. Wahhaj, Z. *et al.* The inner rings of β Pictoris. *Astrophys. J.* **584**, L27–L31 (2003).
9. Malfait, K. *et al.* The spectrum of the young star HD100546 observed with the Infrared Space Observatory. *Astron. Astrophys.* **332**, L25–L28 (1998).
10. Honda, M. *et al.* Detection of crystalline silicates around T Tauri star Hen3–600A. *Astrophys. J.* **585**, L59–L63 (2003).
11. Campins, H. & Ryan, E. V. The identification of crystalline olivine in cometary silicates. *Astrophys. J.* **341**, 1059–1066 (1989).
12. Knacke, R. F. *et al.* The silicates in the disk of beta Pictoris. *Astrophys. J.* **418**, 440–450 (1993).
13. Hallenbeck, S. L., Nuth, J. A. III & Nelson, R. N. Evolving optical properties of annealing silicate grains from amorphous condensate to crystalline mineral. *Astrophys. J.* **535**, 247–255 (2000).
14. Kataza, H. *et al.* COMICS: the cooled mid-infrared camera and spectrometer for the Subaru telescope. *Proc. SPIE* **4008**, 1144–1152 (2000).
15. Okamoto, Y. K. *et al.* Improved performances and capabilities of the Cooled Mid-Infrared Camera and Spectrometer (COMICS) for the Subaru Telescope. *Proc. SPIE* **4841**, 169–180 (2003).
16. Sako, S. *et al.* Improvements in operating the Raytheon 320x240 pixel Si:As impurity band conduction mid-infrared array. *Publ. Astron. Soc. Pacif.* **115**, 1407–1418 (2003).
17. Koike, C. *et al.* Compositional dependence of infrared absorption spectra of crystalline silicate II. Natural and synthetic olivines. *Astron. Astrophys.* **399**, 1101–1107 (2003).
18. Dorschner, J., Begemann, B., Henning, Th., Jäger, C. & Mutschke, H. Steps toward interstellar silicate mineralogy. II. Study of Mg–Fe-silicate glasses of variable composition. *Astron. Astrophys.* **300**, 503–520 (1995).

19. Artymowicz, P. Radiation pressure forces on particles in the Beta Pictoris system. *Astrophys. J.* **335**, L79–L82 (1988).
20. Mukai, T. & Giese, R. H. Modification of the spatial distribution of interplanetary dust grains by Lorentz forces. *Astron. Astrophys.* **131**, 355–363 (1984).
21. Fabian, D., Jäger, C., Henning, Th., Dorschner, J. & Mutschke, H. Steps toward interstellar silicate mineralogy V. Thermal evolution of amorphous magnesium silicates and silica. *Astron. Astrophys.* **364**, 282–292 (2000).
22. Pantin, E., Waelkens, C. & Malfait, K. *The Universe as Seen by ISO* (eds Cox, P. & Kessler, M. F.) 385–388 (ESA SP 427, ESA Publications Division, Noordwijk, 1999).
23. Fixsen, D. J. & Dwek, E. The zodiacal emission spectrum as determined by COBE and its implications. *Astrophys. J.* **578**, 1009–1014 (2002).
24. Backman, D. E., Witteborn, F. C. & Gillett, F. C. Infrared observations and thermal models of the Beta Pictoris disk. *Astrophys. J.* **385**, 670–679 (1992).
25. Weinberger, A. J., Becklin, E. E. & Zuckerman, B. The first spatially resolved mid-infrared spectroscopy of β Pictoris. *Astrophys. J.* **584**, L33–L37 (2003).

Acknowledgements This Letter is based on data collected at the Subaru Telescope, which is operated by the National Astronomical Observatory of Japan. We thank C. Koike, I. Yamamura, F. Usui, S. Hasagawa, T. Ootsubo, H. Chihara, T. Nakamoto, H. Tanaka and T. Takeuchi for comments and discussions.

Competing interests statement The authors declare that they have no competing financial interests.

Correspondence and requests for materials should be addressed to Y.K.O. (okamtoys@cc.nao.ac.jp).

Magnesium sulphate salts and the history of water on Mars

David T. Vaniman¹, David L. Bish², Steve J. Chipera¹, Claire I. Fialips¹, J. William Carey¹ & William C. Feldman³

¹Los Alamos National Laboratory (LANL), MS D462, Los Alamos, New Mexico 87545, USA

²Indiana University, 1001 E 10th St, Bloomington, Indiana 47405, USA

³Los Alamos National Laboratory (LANL), MS D466, Los Alamos, New Mexico 87545, USA

Recent reports of ~ 30 wt% of sulphate within saline sediments on Mars^{1,2}—probably occurring in hydrated form³—suggest a role for sulphates in accounting for equatorial H₂O observed in a global survey by the Odyssey spacecraft⁴. Among salt hydrates likely to be present³, those of the MgSO₄ \cdot nH₂O series have many hydration states. Here we report the exposure of several of these phases to varied temperature, pressure and humidity to constrain their possible H₂O contents under martian surface conditions. We found that crystalline structure and H₂O content are dependent on temperature-pressure history, that an amorphous hydrated phase with slow dehydration kinetics forms at $< 1\%$ relative humidity, and that equilibrium calculations may not reflect the true H₂O-bearing potential of martian soils. Mg sulphate salts can retain sufficient H₂O to explain a portion of the Odyssey observations⁵. Because phases in the MgSO₄ \cdot nH₂O system are sensitive to temperature and humidity, they can reveal much about the history of water on Mars. However, their ease of transformation implies that salt hydrates collected on Mars will not be returned to Earth unmodified, and that accurate *in situ* analysis is imperative.

Direct evidence for sulphate salts on Mars dates back to recognition of an Mg–S correlation in X-ray fluorescence data collected by Viking in 1976 at two widely separated landing sites⁶. The Viking data led to the concept of Mg sulphate salt as a widespread cementing agent at ~ 10 wt% (anhydrous basis) in martian soils⁷, particularly as a shallow ‘duricrust’ within the upper few centimetres of soil. The concept of widespread Mg sulphate salt distribution in soils was reinforced by detection of similar Mg–S

correlations at the Pathfinder landing site in 1997 (refs 8, 9), and by recent determination of comparable Mg–S compositions in soils and within a possible coating of cemented dust on the rock Mazatzal at Gusev crater¹⁰. Global thermal inertia data¹¹ and thermal emission spectroscopy¹² suggest that duricrust may cover vast tracts of land at the martian equator. Widespread distribution of sulphate salt as a cementing agent in soil may be attributed to a relatively young pedogenic process, possibly acidic weathering, that does not require surface water or ground water^{13,14}. A pedogenic origin remains plausible for this particular mode of occurrence, but results from the Mars Exploration Rover Opportunity at Meridiani Planum^{1,2} provide compelling evidence that sediments rich in sulphate salts formed on Mars by evaporation from water.

The Odyssey orbiter has recently provided global maps of water-equivalent hydrogen that reveal surprisingly high abundances of near-surface hydrogen (~ 9 –11 wt% H₂O equivalent¹⁵) in widespread equatorial regions where water ice is unstable to sublimation¹⁵. The observed H suggests the presence of hydrous silicates or salt hydrates in the upper 1 m of regolith^{16,17}. It has been known since Viking that lesser amounts of Cl and minor amounts of Br are associated with S, and the hydroxylated K–Fe³⁺ sulphate mineral jarosite (20% OH; 11% H₂O equivalent) has been found at Meridiani Planum¹, all of which point to a complex salt assemblage for which many possible mineralogies have been suggested¹⁸. Nevertheless, the widespread Mg–S association observed by Viking, Pathfinder and the MER rovers indicates that some form of MgSO₄ \cdot nH₂O is common in soils that are globally distributed on Mars.

The only common, naturally occurring members of the MgSO₄ \cdot nH₂O series on Earth are epsomite (MgSO₄ \cdot 7H₂O, 51 wt% water), hexahydrite (MgSO₄ \cdot 6H₂O, 47 wt% water) and kieserite (MgSO₄ \cdot H₂O, 13 wt% water). These three salts are believed to be the only members that occur on Earth as thermodynamically stable minerals¹⁹. Rare, metastable minerals of the series include pentahydrite (MgSO₄ \cdot 5H₂O, 43 wt% water), starkeyite (MgSO₄ \cdot 4H₂O, 37 wt% water) and sanderite (MgSO₄ \cdot 2H₂O, 23 wt% water). Other hydration states ($n = 12, 3, 1.25$) are not recognized as minerals but can be synthesized. All of these salts consist of SO₄ tetrahedra and Mg(O,H₂O)₆ octahedra; some include extra-polyhedral water (water that is not in octahedral coordination with Mg)²⁰. Epsomite transforms readily to hexahydrite by loss of extra-polyhedral water; this transition is reversible and occurs at ~ 50 –55% relative humidity (RH) at 298 K and at lower temperatures as the activity of water diminishes¹⁹. Kieserite is more stable at lower RH and higher temperature; for example, at moderate heating rates in thermogravimetric analysis the kieserite structure survives to ~ 670 K, compared with ~ 450 K for hexahydrite. However, as we show here, kieserite converts to hexahydrite or epsomite as humidity increases, yet these phases do not easily revert to kieserite on desiccation. Metastability, kinetic effects and pathway dependence are important factors in the MgSO₄ \cdot nH₂O system.

We have examined formation and transformation of MgSO₄ \cdot nH₂O minerals precipitated by evaporation from MgSO₄ solutions or transformed in the solid state under conditions of controlled temperature and humidity. These experiments include formation at conditions of ~ 1 torr total pressure, which is slightly less than Mars’ atmospheric pressure (~ 5 torr at most equatorial elevations). Other experiments have been conducted¹⁷ at temperatures from 100 to 298 K, and from 10^{-5} torr to ambient pressure (~ 580 torr in our laboratory at 2,265 m elevation). In addition, we have used thermogravimetric analysis (TGA) and isothermal controlled-humidity gravimetric analysis to examine water gain and loss from MgSO₄ \cdot nH₂O samples. Our most extensive data consist of X-ray diffraction (XRD) analyses collected while samples were held in an environmental cell²¹ at controlled RH and ambient temperature (~ 298 K) inside the diffractometer.